Part II

Laminar Flame Dynamics Studies

Chapter 4

Self-Excited Combustion: Rijke Tube Combustor

Stringent emissions standards imposed in recent years have led to the design and installation of lean, premixed gas turbine combustors. In these type of combustors structural failure may take place because of thermoacoustic combustion instabilities which occur at various operating ranges including lean conditions. The occurrence of these thermoacoustic instabilities is characterized by large acoustic pressures (RMS) inside the combustion chamber. To be able to prevent the instabilities from happening or to control them, there is need to understand controlling mechanisms and to develop capabilities for prediction of the conditions under which they occur.

4.1 Rationale and Objectives

The Rijke tube combustor provides an elementary example of thermoacoustic oscillation with heat release from the flame (which is anchored on a grid inside the tube) as a source of excitation. There are some important limitations associated with the study of thermoacoustic

instabilities in Rijke tubes versus real, full-scale combustors. Primarily, the fluid dynamic coupling is not important, as there are no vortical structures in the tube flow that can cause periodic heat release. This simplifies the study of the features that were the focus of the present study. Specifically, the tube combustor was intentionally selected to eliminate coupling between thermoacoustic instabilities and flow instabilities. There is a large amount of information that resides in the spectral representations of any dynamic system response measurements for linear or nonlinear systems. The information supports descriptions of physical phenomena responsible for unique spectral features. Therefore, by analyzing the Rijke tube it is helpful to discern the details of the thermoacoustic pressure signatures for both dynamic modeling and system monitoring in any combustor system.

Experimental studies and theoretical modeling of the Rijke tube have been previously undertaken [44, 45]. A one-dimensional initial value problem approach was chosen by Nark and Hardin [46] whereas Yoon et al [47] used modal analysis to produce a linear velocity sensitive thermoacoustic response model. Recently, Nord [48] conducted both experimental and theoretical studies on a tube combustor similar to a Rijke tube and proposed three distinct mechanisms affecting the acoustic pressure in the tube. The three mechanisms are: a main thermoacoustic instability in accordance to the Rayleigh Criterion [36]; a vibrating flame instability where the flame sheet exhibits mode shapes; and a pulsating thermodiffusive instability driven by heat losses to the flame stabilizer. The study was based on acoustic pressure and chemiluminescence observations in the frequency domain and helped gain understanding of the complex coupling mechanism between unsteady heat release and acoustics in the combustor.

Both experimental studies on and analytical modeling of Rijke tubes have been conducted for a very long time (see review by Raun et al. [49] and the book by Putnam [50]). Numerical modeling, especially Computational Fluid Dynamics (CFD) based modeling, has been more recently reported. Yan [51] used second-order accurate schemes to simulate two-dimensional self-excited oscillating flows in a Rijke tube configuration. The combustion process was substituted by the presence of a heat source, in effect eliminating the possibility of capturing

the thermo-diffusive instability (the pulsating flame instability mentioned earlier) which is due to the heat transfer interaction between the flame stabilizer and the flame. Also, a sinusoidally time varying energy release from the heat source was assumed. A range of forcing frequencies were chosen to determine the optimal frequency (matching the natural frequency of the structure) of the simulation through pressure wave numbers. They used specialized numerical schemes [52] to capture propagation of pressure and shock waves in the high Mach number ($Ma \leq 0.8$) flow regime.

Another similar one-dimensional study using a heat source and heat sink pair was conducted by Ishii et al. [53]. A steady heat supply was maintained to the heat source and the heat flux into the fluid (assumed to be an ideal gas) was allowed to fluctuate because of the velocity variation. This variation was explained with a hypothesis that because of the steep thermal gradient between the heat source and the heat sink, thermal energy was getting transformed into mechanical energy (heat-induced vibration). Such a phenomena is different from thermoacoustic driving mechanism and hence the model can not be of help in understanding combustion instabilities.

Entezam et al. [54] have used FLOW-3D software [55] to simulate flow in a Rijke tube. A solid porous obstacle was used as the heat source with a step-input chosen for the heat release. In another article [56] the authors apply dimensional analysis to create a similarity parameter relating the oscillating heat flux to pressure, velocity and a characteristic length. Perhaps the most comprehensive CFD study of thermoacoustic instabilities in Rijke tubes has been conducted by Sangyeon et al. [57]. Attention was given to the fundamental mode in the tube rather than the higher modes of oscillation. Single-step propane-air global reaction mechanism to simulate chemical reaction and k-ε turbulence modeling were incorporated using the KIVA-II code [58]. The honeycomb flame-holder present in the associated experimental study was not considered for the simulation and forced oscillation was used as a triggering mechanism to simulate unsteady behavior of the flow.

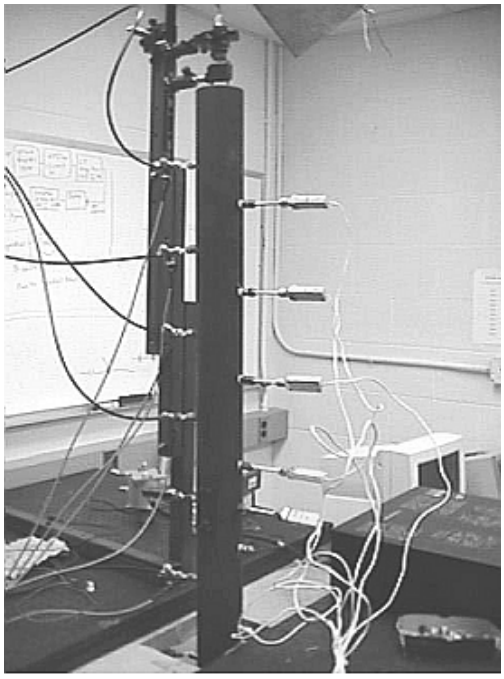

Figure 4.1: The Rijke tube combustor

4.2 Technical Approach

The present study aims at the simulation of the thermoacoustic phenomena as well as the thermo-diffusive instability in a Rijke type tube combustor. The modeling effort has been directed toward capturing the physics of the coupling mechanism between acoustics and the unsteady heat release rate of the flame. The Navier-Stokes equations are solved using accurate numerical integration and time-marching schemes, partially-reflecting boundary conditions and finite rate chemistry. A commercial code, FLUENT [59], was used and a two-dimensional simplification of the Rijke tube experimental setup [60] was considered for the CFD study. A multi-passage honeycomb structure was included in the grid to capture the pulsating flame instability. Instead of attempting to model the heat source (for e.g. imposed time-varying heat source), the aim has been to capture the flame-honeycomb heat transfer coupling process which is critical for proper presentation of physics. This inclusion sets apart the present study from the attempts carried out earlier basically because the

flame-honeycomb coupling is modeled accurately instead of considering time varying heat sources or artificially created temperature gradients.

4.3 Accompanying Experimental Studies

A very simple combustion process was selected to facilitate initial studies of thermoacoustic instabilities by the Virginia Active Combustion Control Group (VACCG) at Virginia Tech. A carbon steel tube combustor (as seen in Figure 4.1) $5\,ft$ $(1.524\,m)$ in length and $2.85\,in$ $(7.239\,cm)$ inner diameter was built [60]. Premixed methane-air mixture coming from a gas mixer was fed into the bottom part of the combustor through copper tubes with small holes drilled in the cylindrical shaper tubes. The combustor setup can be seen in Figure 4.2. The main goal of the experimental study was to provide an accurate acoustic pressure measurements toward modeling efforts - identification of reduced-order modeling schemes: energy methods relying on Rayleigh's integral criteria, analytical description of conservation equations, and numerical solutions.

The ceramic honeycomb (Cordierite [SiO_2-Al_2O_3-MgO]) used for stabilization of the laminar flame is shown in Figure 4.3. The flame stabilizer, with an area restriction of approximately 50%, was mounted half way from the bottom of the tube combustor for excitation of the 2nd acoustic mode. The tube combustor is similar to a Rijke tube except that the boundary conditions are closed-open versus open-open for a Rijke tube. According to the Rayleigh Criterion [36] this leads to a thermoacoustic instability of the 2nd acoustic mode when the flame is placed at the middle of the tube. For temperature measurement seven Type K thermocouples were inserted through the combustor wall with the bead located on the centerline of the combustor. The data was processed in a data acquisition PC. For pressure measurements, pressure transducers were mounted on the opposite side of the thermocouples as well as at the bottom of the combustor. The transducers were connected to a strain gage amplifier and conditioner. The data was processed in a dynamic signal analyzer. For chemiluminescence

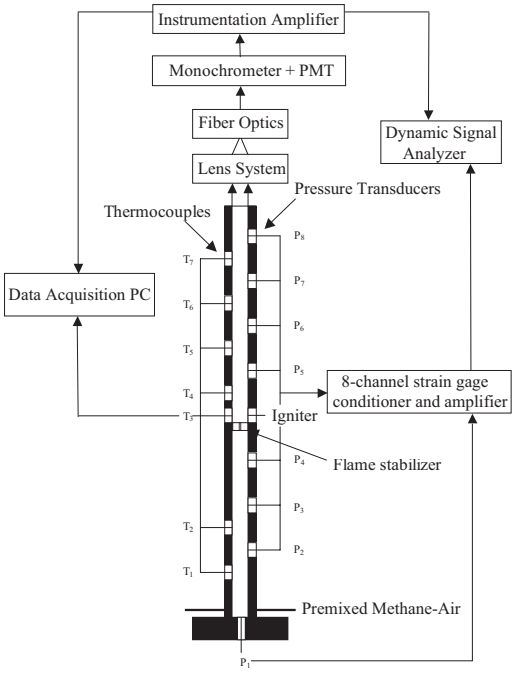

Figure 4.2: The Rijke tube combustor schematic showing the instrumentation

measurements of the flame, an optical system was utilized, which consisted of lenses, fiber optic cable, monochromator and a photomultiplier tube (PMT). The signal from the PMT was amplified and analyzed with a dynamic signal analyzer.

Acoustic signature of the pressure exhibits useful information of the system and it can help to identify reduced-order schemes that provide adequate prediction capabilities for the occurrence and control of thermoacoustic instabilities. Chemiluminescence measurements yielded qualitative magnitudes of unsteady heat release and a phase relationship between unsteady heat release and pressure was established. A typical pressure spectrum of the combustor is shown in Figure 4.4. In the pressure spectrum several regions can be identified:

1. Around $180\,Hz$ a limit-cycle oscillation can be observed. In our case, the second acoustic mode of the combustor goes unstable in agreement with the Rayleigh criterion (described earlier). Also, the harmonics of the limit-cycle are visible in the spectrum.

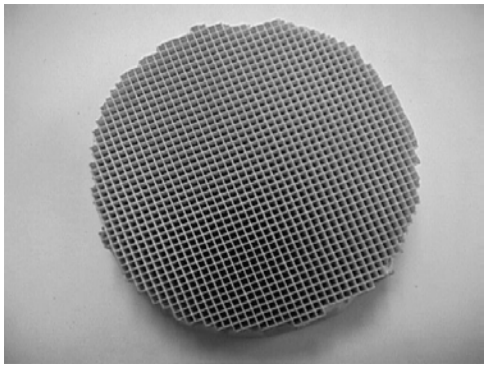

Figure 4.3: Ceramic honeycomb used as a flame holder in the Rijke tube combustor

2. A peak can be observed at half the limit-cycle frequency. The hypothesis is that an oscillation of the flame sheet occurs with double the period of the forcing function which in our case is a pulsation of the acceleration of the gas column surrounding the flame.

3. A low frequency peak (between 10-20 Hz) is also visible in Figure 4.4. This is the pulsating flame instability which was mentioned earlier. This subsonic frequency is responsible for modulating other peaks in the spectrum.

The following sub-section includes the description of the different features mentioned above.

4.3.1 Limit-Cycle and Harmonics

In certain non-linear systems a self excited oscillation, or a limit-cycle occurs. For example, in the following equation for a mass-spring-damper system:

$$m\ddot{x} - c\left(1 - x^2\right)\dot{x} + kx = 0 \tag{4.1}$$

m is the mass, $c\,(1 - x^2)$ is the damping term and k the stiffness of the system. For small values of x the damping will be negative and will put energy into the system, but for large values of x, the damping will be positive and energy will be removed from the system. At some displacement amplitude ($|x|$), the system will reach a limit-cycle because of the

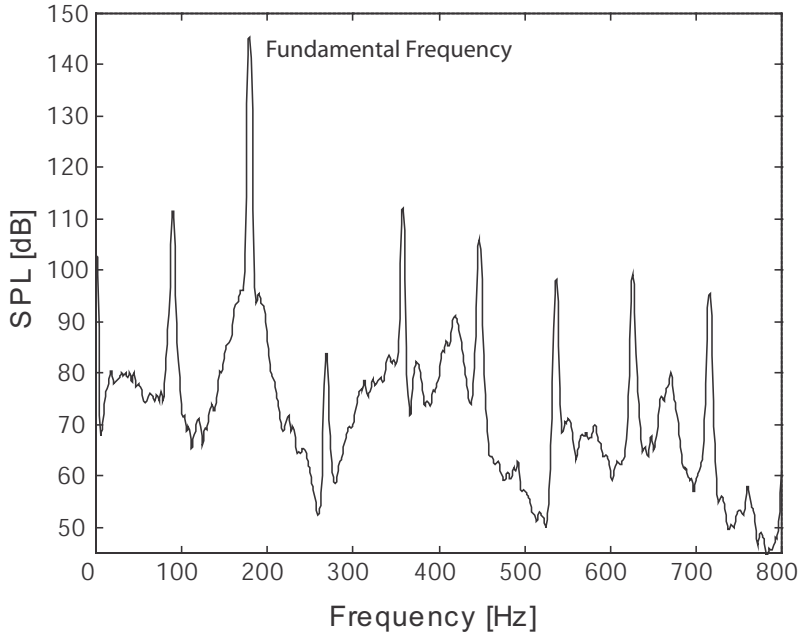

Figure 4.4: Pressure power spectrum from Rijke tube experiment ($\phi = 0.6$, $Q = 120\,cc/s$)

damping term. A similar limit-cycle behavior is observed in the tube combustor, where the second acoustic mode gets excited. In Figure 4.5, the limit-cycle frequency can be observed.

4.3.2 Subharmonic Response

Markstein [61], using perturbation methods, modeled the distortion of the flame front as a second order oscillator. He showed that there is a region of instability which renders flame oscillations at half the frequency of the parametric (acoustic) forcing. It is possible that such a flame instability drives the acoustics, leading to subharmonic resonances of pressure. When the flame sheet oscillates, the flame surface area changes and since the heat release is proportional to the flame surface area, the heat release also oscillates. In addition, as the flame oscillates, the heat loss to the flame stabilizer and the combustor walls changes which

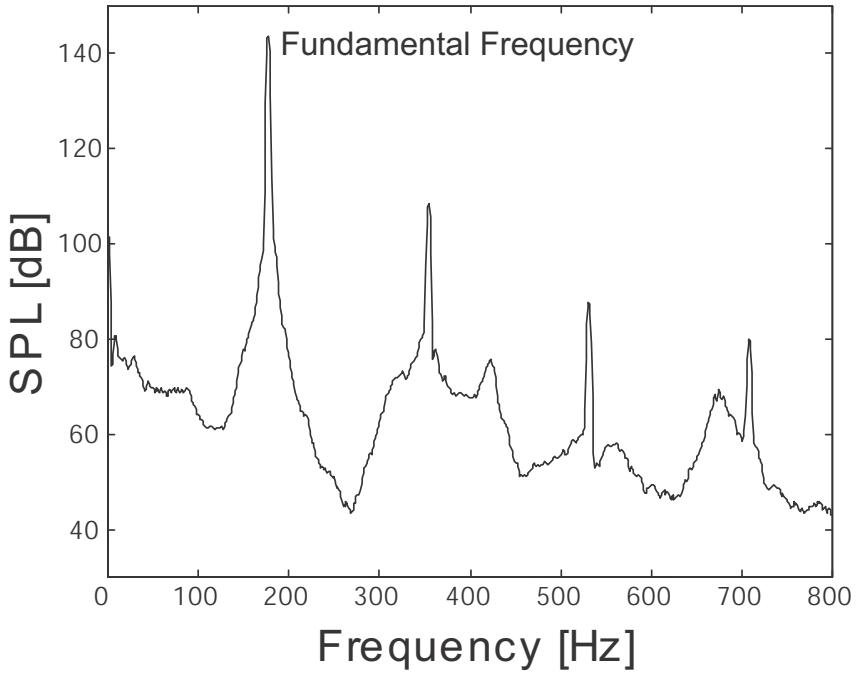

Figure 4.5: Power spectrum of limit-cycle from Rijke tube experiment ($\phi = 0.5$, $Q = 160\,cc/s$)

leads to a change in the net heat input to the gas. This change in heat release couples with the acoustic particle velocity and therefore we see a subharmonic peak (Figure 4.6 shows closeup of the peak) at half the limit-cycle frequency in the pressure power spectrum.

To determine if this feature in the tube combustor is the same as Markstein described, experiments were conducted to dampen the thermoacoustic instability as well as shift the frequency of the instability to check the effect on subharmonic response magnitude and frequency. It was noted that the level of the thermoacoustic instability affects the subharmonic instability. For a certain frequency of the limit-cycle, there is a threshold minimum amplitude that the limit-cycle must have to drive the subharmonic instability. This minimum amplitude value changes according to the change in the frequency of limit-cycle and the flame-sheet seems to have preferred frequencies which can be seen as resonances of the flame (mode shapes).

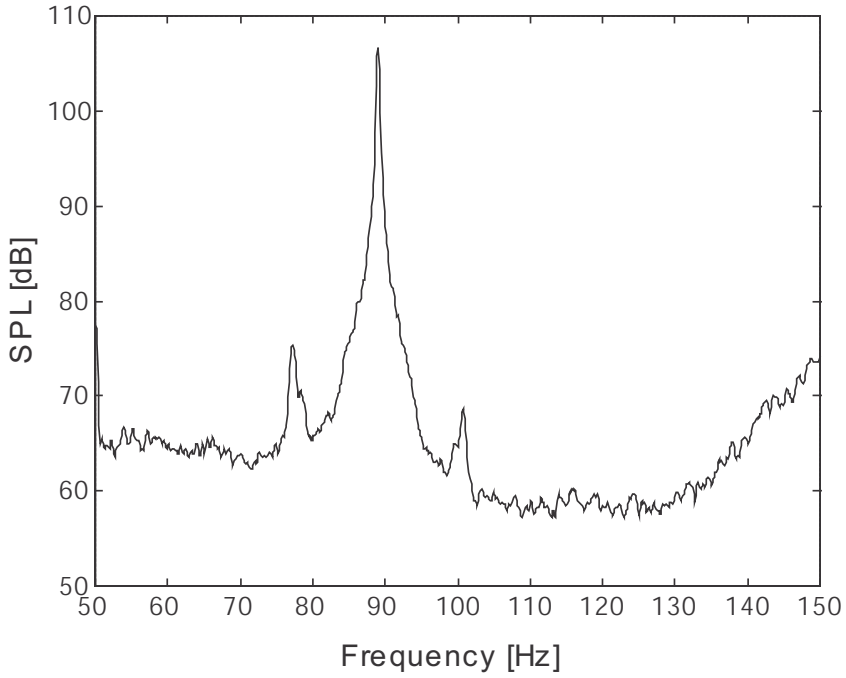

Figure 4.6: The subharmonic response from Rijke tube experiment ($\phi = 0.6$, $Q = 120\,cc/s$)

4.3.3 Subsonic Instability

At higher equivalence ratios ($\phi > 0.65$) the thermoacoustic instability shows evidence of amplitude modulation. The characteristic sidebands ($\pm$10-20 Hz) are evident throughout the spectrum but are especially obvious around the subharmonic and fundamental limit-cycle frequencies. This energy is related to a 'pulsating instability' as defined by Margolis [62] and is a type of thermal-diffusive instability that promotes the flame-sheet to move toward and away from the burner periodically, thereby modulating the overall rate of change of heat input to the acoustic mode. In the tube combustor, the frequencies for this pulsating flame instability has been observed to lie between $10\,Hz$ and $20\,Hz$. With increasing equivalence ratio, an increase in the amplitude and frequency of the instability can be observed (Figure 4.7).

This subharmonic response of the flame is observed to cause an amplitude modulation of the

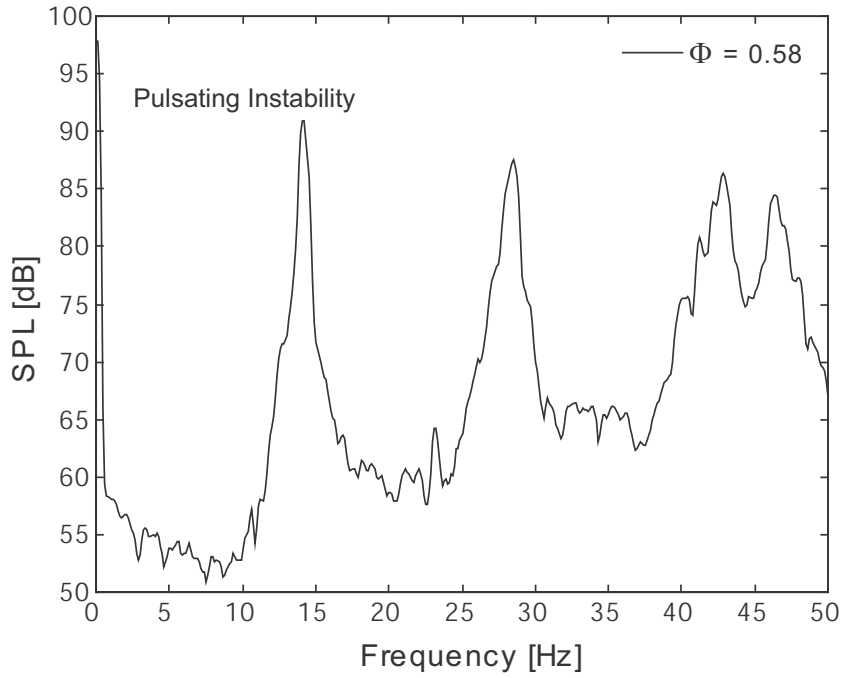

Figure 4.7: Pressure power spectrum from Rijke tube experiment, showing pulsating flame instability

limit-cycle, the subharmonic response and the harmonics. Figure 4.8 shows the amplitude modulation (marked by 'AM' in the figure). The results strengthen the pulsating instability theory because of the following reasons:

1. The frequency range observed in the tube combustor is in the same range as described in Margolis' theory [62].

2. Increase in equivalence ratio increases the frequency of the pulsating instability. This is also suggested in the theory since an increase in the equivalence ratio increases the flame temperature which results in higher flame speed. The higher flame speed overcomes the effect of forced convection (unburned mixture flow), the flame moves closer to the flame-stabilizer and thus the frequency increases.

In summary, there are numerous effects which can be observed in the response of the self-

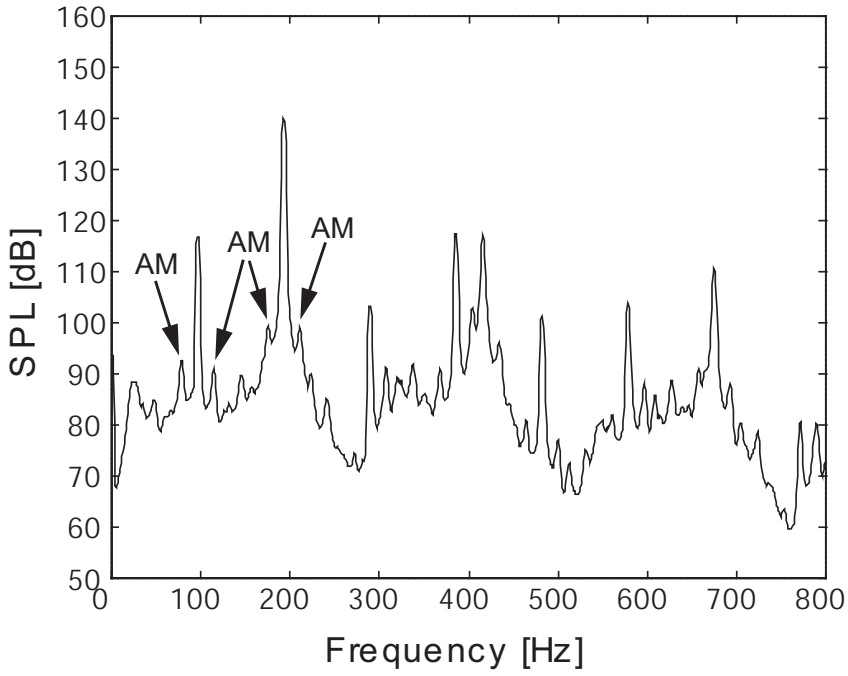

Figure 4.8: Pressure power spectrum from Rijke tube experiment, showing amplitude modulation of the fundamental (AM) – $\phi = 0.65$

excited combustion process. These include the fundamental thermoacoustic limit-cycle and associated harmonic responses, the subharmonic response, a low-amplitude, subsonic limit-cycle response, and the modulation product responses (see Figure 4.9). The experimental study showed that there is coupling between flame instabilities and thermoacoustic instabilities.

4.4 Computational Model

A two-dimensional representation of the Rijke tube apparatus (shown in Figure 4.2) has been used for simulating the reacting flow. The computational geometry used in the solution process is illustrated in Figure 4.10 with the thicker lines, and the actual internal geometry of the tube is shown by the thinner lines. The honeycomb structure can be seen positioned

Peak - Description
1 - pulsating instability
2 - $f_{LC}/4$
3 - lower AM sideband
4 - subharmonic ($f_{LC}/2$), $2f_{LC}/4$
5 - upper AM sideband
6 - $3f_{LC}/4$
7 - lower AM sideband
8 - f_{LC}, TA instability
9 - upper AM sideband
10 - $5f_{LC}/4$
11 - $3f_{LC}/2$, $6f_{LC}/4$
12 - upper AM sideband
13 - $7f_{LC}/4$
14 - lower AM sideband
15 - $2f_{LC}$, $4f_{LC}/2$, $8f_{LC}/4$
16 - upper AM sideband

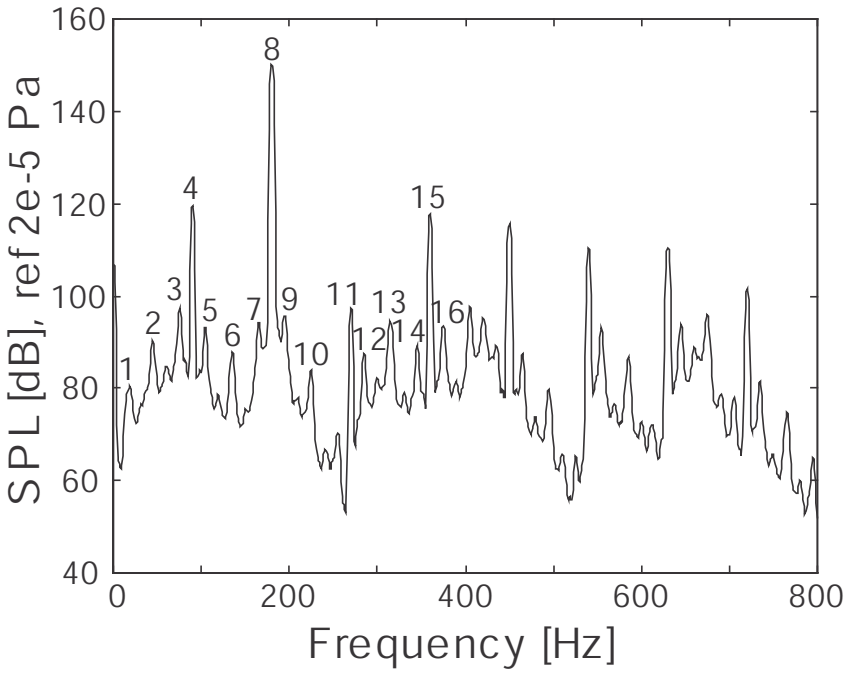

Figure 4.9: Pressure power spectrum for $\phi = 0.65$, $Q = 120\,cc/s$ and peak descriptions

middle of the tube and various boundaries of the geometry have been labled.

4.4.1 Computational Geometry and Grid Generation

The inlet of the tube is a simplification of the closed-bottom inlet of the experimental apparatus described in Section 4.3. The honeycomb is positioned at the center of the $5\,ft$ ($1.524\,m$) tube and has a thickness of $1\,in$ ($2.54\,cm$). The three-dimensional square honeycomb channels have been approximated by two-dimensional channels with alternating solid and fluid sections in the computational geometry (as shown in Figure 4.11). The centerline, outlet and wall constitute the rest of the computation space.

While generating the grid, the following two points were taken into consideration:

1. Since the computational geometry has a very high length to diameter ratio, the number of grid points needed to accurately capture the flow field is going to be high. The key

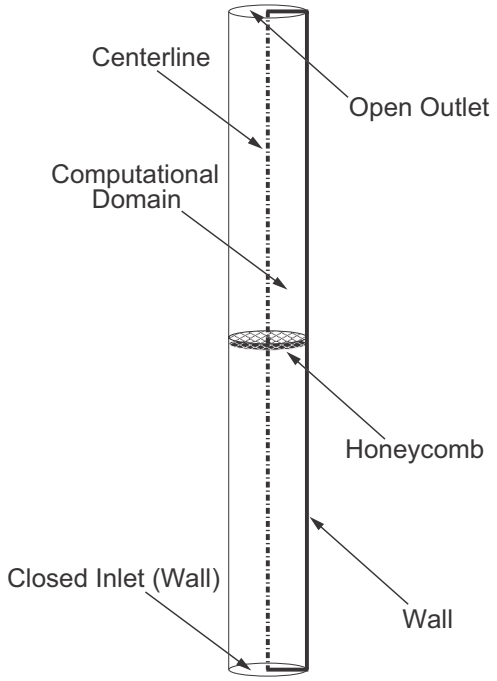

Figure 4.10: Rijke tube computational geometry (not to scale)

to reducing the number of grid points lies in decoupling the honeycomb flame-stabilizer grid from both the upstream and downstream lengths of the combustor.

2. Decoupling the honeycomb grid from other flow areas of the geometry introduces coarse grid cells immediately downstream of the honeycomb. To capture the laminar flat flame that anchors on top of the honeycomb, the coarse grid needs to be adapted to finer grid cells.

A hybrid – structured (quadrilateral) and unstructured (triangular) – grid was therefore generated using the GAMBIT 1.0 grid generation program [59]. The unstructured part of the grid was confined to the upstream and downstream of the honeycomb. To make the grid size outside the honeycomb independent of the grid inside the honeycomb, such a transition between structured and unstructured grid regions was necessary.

The upstream portion of the grid is structured, followed by unstructured grid just upstream of

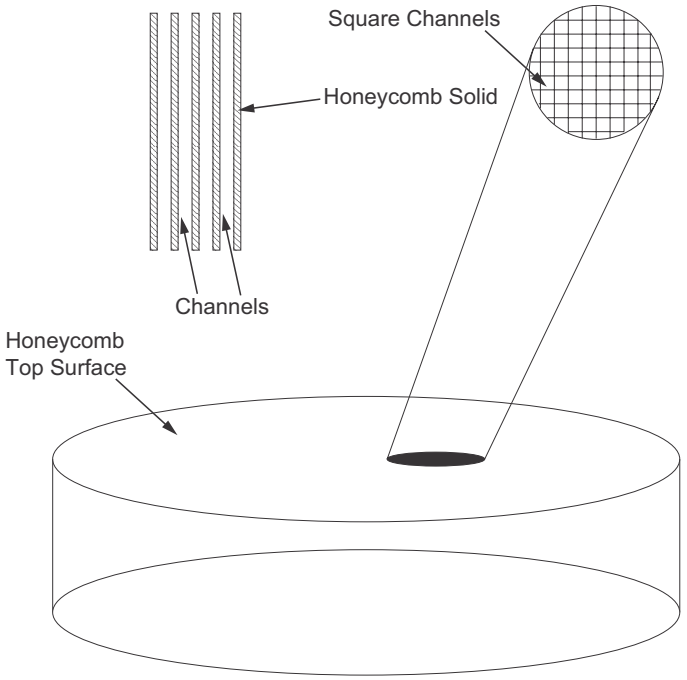

Figure 4.11: Two-dimensional Rijke tube honeycomb channels approximation (not to scale)

the honeycomb. A similar structure of the grid was imposed downstream of the honeycomb. The grid near the flame location (downstream of the honeycomb) is shown in Figure 4.12 and the transition from quadrilateral grid inside the honeycomb to triangular in the flame region and subsequently back to quadrilateral grid further downstream is illustrated.

4.4.2 Flow Modeling

Two-dimensional unsteady Navier-Stokes equations along with the continuity equation, energy equation and chemical reaction equations have been solved using the Fluent 5.1-5.3 segregated solver (FLUENT/UNS [63]). Mixing and transport of species was modeled by solving conservation equations describing convection, diffusion, and reaction sources for each component species. The local mass fraction of each species, $Y_{i'}$ is predicted through the

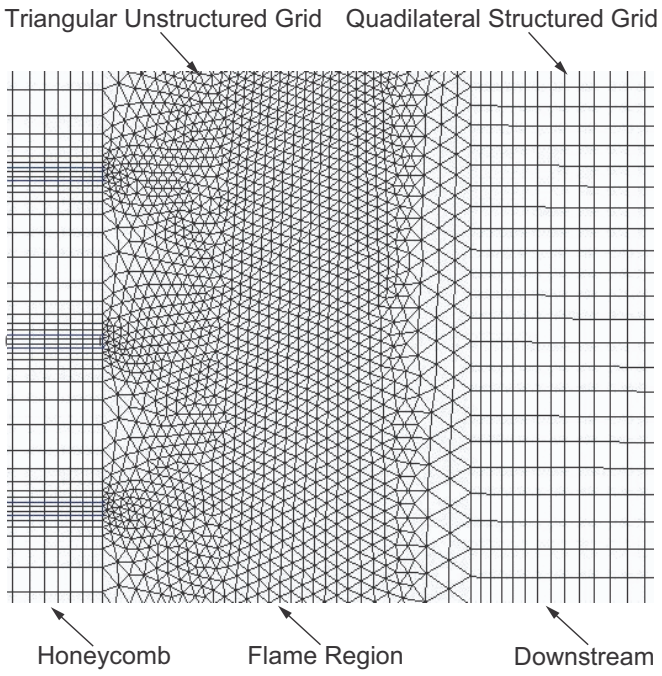

Figure 4.12: Grid inside the Rijke tube honeycomb passages – flame region and downstream

solution of the following conservation equation for the i'th species:

$$\frac{\partial}{\partial t}\left(\rho Y_{i'}\right) + \frac{\partial}{\partial x_i}\left(\rho u_i Y_{i'}\right) = -\frac{\partial}{\partial x_i} J_{i',i} + R_{i'} \tag{4.2}$$

where $R_{i'}$ is the mass rate of creation or depletion of species by chemical reaction. Four such equations are solved for the four species (CH_4, O_2, CO_2 and H_2O) and along with N_2 there are five fluid phase chemical species present in the system. $J_{i'}$ is the diffusion flux of species i', which arises due to concentration gradients. The diffusion flux is calculated using the dilute approximation (Fick's law):

$$J_{i',i} = -\rho D_{i'} \frac{\partial Y_{i'}}{\partial x_i} \tag{4.3}$$

here $D_{i'}$ is the diffusion coefficient for species i' in the mixture. Since in multicomponent mixing flows the transport of enthalpy due to species diffusion can have a significant effect on the enthalpy field, the following term:

$$\nabla \cdot \left[\sum_{i'=1}^{n} \left(h_{i'}\right) J_{i'}\right] \tag{4.4}$$

is included in the energy equation. The source of energy term, S_h, which is added to the energy equation, includes the source of energy due to chemical reaction ($S_{h,reaction}$):

$$S_{h,reaction} = \sum_{j'} \left[\frac{h^0_{j'}}{M_{j'}} + \int_{T_{ref_{j'}}}^{T_{ref}} c_{p,j'} dT \right] R_{j'} \tag{4.5}$$

where $h^0_{j'}$ is the enthalpy of formation of species j' and $R_{j'}$ is the volumetric rate of creation of species j'.

A first-order implicit formulation in time along with second order accurate spatial discretization were used in the solution process. A time step of $1.22 \times 10^{-5}\, s$ was chosen to capture the time varying pressure fluctuations. A second-order accurate scheme was used for pressure interpolation. The scheme reconstructs cell face pressure in a similar manner as is done with second-order accurate convection terms in the Navier-Stokes equation. Second-order accurate upwind schemes have been used for momentum, species and in the energy equation whereas a first-order accurate scheme was used for calculating density. PISO (Pressure-Implicit with Splitting of Operators) scheme has been used for pressure-velocity coupling. This scheme was opted for instead of SIMPLE/SIMPLEC because of its ability to insure faster prediction of corrected velocity field for unsteady calculations. The neighbor correction option, which in effect is responsible for the reduced number of iterations to reach convergence, was chosen and the skewness correction option was also opted for to account for the skewness in the triangular grid cells (downstream of the honeycomb flame stabilizer). An iterative process similar to the neighbor correction method was used to reduce convergence difficulties associated with the distorted mesh downstream of the honeycomb.

The global convergence criteria was set at 10^{-4} for momentum and continuity residuals and 10^{-6} for energy and species concentrations. An average of 8 iterations were needed per time-step for convergence criteria to be satisfied. Average time taken per time-step was around $60\, s$ on a SGI Origin 2000 machine (32 195 MHz R12000 processors, 20 GB memory) using 8 processors at a time. Convergence difficulties were encountered in a previous attempt [64] at using the coupled solver of FLUENT to simulate the reacting flow in the combustor. The solution method of the coupled solver (FLUENT/RAMPANT [63]) ensures stronger coupling

between the species solver and the main fluid flow solver, but was ineffective at solving the stiff set of equations resulting from the use of the single-step chemistry model. Although, using the segregated solver the initial solution was achieved using low relaxation factors for energy and density updates, the unsteady solution converged faster for each time-step and high relaxation factors (close to 1 for energy and density) were implemented.

4.4.3 Chemistry and Heat Transfer Modeling

The single-step expression given in Equation 4.6 has been used for the global reaction of methane and air:

$$CH_4 + 2\left(O_2 + 3.76N_2\right) \xrightarrow{k_G} CO_2 + 2H_2O + 7.52N_2 \tag{4.6}$$

The rate of fuel consumption is given by the global Arhenius equation:

$$\frac{d\left[CH_4\right]}{dt} = -A \exp\left(\frac{-E_a}{R_u T}\right)\left[CH_4\right]^m \left[O_2\right]^n \tag{4.7}$$

where, the parameters A, E_a/R_u, m and n have been chosen to provide best agreement between experimental and predicted flame speeds (Westbrook and Dryer [65]) and are given in Table 4.1.

Table 4.1: Chemistry model for the Rijke tube combustor simulation

Pre-exponential Factor $A\left[(gmol/cm^3)^{1-m-n/s}\right]$	Activation Temperature $[E_a/R_u\,(K)]$	m	n
1.3×10^8	$24,358\ [E_a = 48.4\,kcal/gmol]$	-0.3	1.3

Input Properties

For a standard run of the Rijke tube simulation for a flow rate of $120\,cc/s$ and an equivalence ratio (ϕ) of 1.0, Table 4.2 summarizes the material properties of the tube, honeycomb and

the fluid region. A fixed convective heat transfer coefficient of 20 W/m^2K was imposed for the outer wall of the tube. The honeycomb ceramic (Cordierite) is made up of various components, out of which SiO_2, Al_2O_3 and MgO are the major constituents.

Table 4.2: Material properties used in the Rijke tube simulation

	Unit	Input
Tube Properties		
Material	-	Carbon Steel
Height	m	1.524
Diameter	m	0.07239
Wall Thickness	m	0.00635
Thermal Conductivity	W/mK	16.27
Specific Heat (C_p)	J/kgK	502.48
Density	kg/m^3	8030.0
Convective Heat Transfer Coefficient	W/m^2K	20.0
Honeycomb Properties		
Material	-	Cordierite
Composition	-	SiO_2-Al_2O_3-MgO
Thickness	m	0.0254
Diameter	m	0.07239
Location from bottom	m	0.762
Thermal Conductivity	W/mK	2.28228
Specific Heat (C_p)	J/kgK	850.63
Density	kg/m^3	2300.0

For the species properties, different formulations in FLUENT were chosen. For density of

the mixture ideal gas law is used and the solver computes the density as

$$\rho = \frac{p_{op} + p}{RT \sum_{i'} \frac{m'_i}{M'_i}} \tag{4.8}$$

where R is the universal gas constant, m'_i is the mass fraction of species i', M'_i is the molecular weight of species i', and p_{op} is the operating pressure ($1\,bar$). Therefore, the density depends on the local relative pressure field. The solver computes the viscosity based on kinetic theory for the ideal gas mixture as:

$$\mu = \sum_{i'} \frac{X_{i'} \mu_{i'}}{\sum_{i'} X_{i'} \phi_{i'j'}} \tag{4.9}$$

where

$$\phi_{i'j'} = \frac{\left[1 + \left(\frac{\mu_{i'}}{\mu_{j'}}\right)^{\frac{1}{2}} \left(\frac{M_{j'}}{M_{i'}}\right)^{\frac{1}{4}}\right]^2}{\left[8\left(1 + \frac{M_{i'}}{M_{j'}}\right)\right]^{\frac{1}{2}}} \tag{4.10}$$

and $X_{i'}$ is the mole fraction of species i'. A similar formulation for the mixture thermal conductivity is chosen and is calculated as

$$k = \sum_{i'} \frac{X_{i'} k_{i'}}{\sum_{i'} X_{i'} \phi_{i'j'}} \tag{4.11}$$

where $\phi_{i'j'}$ is the same as in Equation 4.10. The mixture specific heat capacity is computed as a mass fraction average of the pure species heat capacities

$$c_p = \sum_{i'} m_{i'} c_{p,i'} \tag{4.12}$$

The mass diffusion coefficient $\mathcal{D}_{i'j'}$ and the thermal diffusion coefficient are calculated using kinetic theory. Table 4.3 summarizes the modeling of species transport properties.

4.4.4 Boundary and Initial Conditions

The flowfield was initialized by the velocity and mass fraction values of species specified at the inlet of the combustor. Initial cold flow solution was first generated using first order accurate upwinding schemes for velocities, second-order accurate scheme for pressure interpolation and

Table 4.3: Mixture properties modeling formulation and transport properties used in the Rijke tube combustor simulation

	Unit	Modeling Method
Mixture Properties Modeling Formulation		
Density	kg/m^3	Ideal Gas
Specific Heat (C_p)	J/kgK	Mixing Law
Thermal Conductivity	W/mK	Ideal Gas Mixing Law
Viscosity	kg/ms	Ideal Gas Mixing Law
Mass Diffusivity	m^2/s	Kinetic Theory
Thermal Diffusion Coefficient	kg/ms	Kinetic Theory
Species Transport Properties		
Viscosity	kg/ms	Kinetic Theory
Specific Heat (C_p)	J/kgK	Polynomial Function of Temperature

SIMPLE pressure-velocity coupling method. Subsequently, ignition of the fuel-air mixture was initiated by a $3000\,K$ temperature patch on top of the honeycomb flame stabilizer. The energy and density under-relaxation values were initially kept at 0.1 and subsequently increased to 0.5. Finally, second-order accurate upwind schemes were used for velocities, species and energy to generate a reacting flow steady state initial solution.

The closed-bottom acoustic inlet boundary condition was implemented by using a uniform and steady inlet velocity profile. This profile ensured an acoustically closed inlet because of the fluctuating component of velocity being zero ($u' = 0$). The mean velocity as well as methane and oxygen mass fractions were specified at the bottom inlet of the combustor. The density of the incoming mixture was determined by the ideal gas law. A non-reflecting boundary condition was applied at the outlet where the pressure ($\overline{p}$) was fixed at $1\,bar$, thus implementing the open acoustic boundary condition. The walls were treated as convec-

tive boundaries where an outside (ambient air side) heat transfer coefficient was specified. Therefore, the inside wall temperature was determined dynamically every time-step with a dependence on the heat convected by the outer wall to the ambient. The honeycomb walls were coupled to both the solid regions of the honeycomb ceramic and the fluid flow passages. This coupling ensured heat transfer between the fluid and the solid regions of the honeycomb passages. A symmetry boundary was chosen for the centerline. The symmetry boundary condition helped reduce the number of grid points by half, in effect reducing computation time. The boundary conditions are summarized in Table 4.4.

Table 4.4: Boundary conditions for the Rijke tube combustor simulation

Boundary	Boundary Condition
Inlet (Closed Wall)	Uniform and steady velocity ($u' = 0$), fuel-air mass fractions, temperature of the mixture
Outlet (Open)	Atmospheric pressure
Combustor walls	Convective heat loss to the atmosphere from the outer wall
Honeycomb walls	Coupled to the adjoining solid and fluid regions

4.5 Results and Discussion

The objective of this part of the study has primarily been to provide a two-dimensional CFD model to capture the thermoacoustic instability occurring in the combustor. To achieve the objective it was needed that the fundamental frequency of the thermoacoustic oscillation be captured with reasonable accuracy. It is demonstrated in this section that the fundamental frequency of oscillation as well as other features of the pressure power spectrum have been captured and their agreement with experimental results prove that the model is able to describe the physics of the reacting flow in the combustor with a high degree of accuracy.

Results are being presented in the form of a comparison between the CFD solution and experimental analysis. The methane-air premix enters the combustor with a flow rate of $120\,cc/s$ and equivalence ratio (ϕ) of 1.0. The incoming temperature of the mixture is $300\,K$. The unsteady pressure fluctuations were recorded at several locations, both upstream and downstream of the honeycomb. Apart from the pressure measurement, temperature distribution along the axial centerline, velocity profile at the flame location, and axial mass fraction distribution of the species are also presented. Unlike the simulation carried out by Cho et al. [57], this simulation does not use the 'instability triggering method' [66] to simulate the coupling mechanism between unsteady heat release and acoustics. Instead, the growth of the instability is captured by the numerical model.

4.5.1 Reacting Flowfield Structure

The reacting flow steady-state solution was used as an initial solution to start the unsteady, time-dependent solution process. The steady state solution included the accurate capture of the flame anchoring process, the consumption of reactants and products formation and steady-state temperature distribution along the combustor. Each process/distribution is important for the validation of the computational results against theory and experimental results.

Flame Anchoring

The flame anchoring process on top of the honeycomb flame-stabilizer is perhaps the most important objective of the simulation. Accurate modeling of the flame anchoring process enables the capture of the thermo-diffusive instability (mentioned in Section 4.3.3) as well as fixes the position of the heat source in the Rijke tube, as required by the Rayleigh's criterion. The CFD model was successfully able to predict the anchoring process. Figure 4.13 shows instantaneous reaction rate contours downstream of the honeycomb. The higher reaction rate

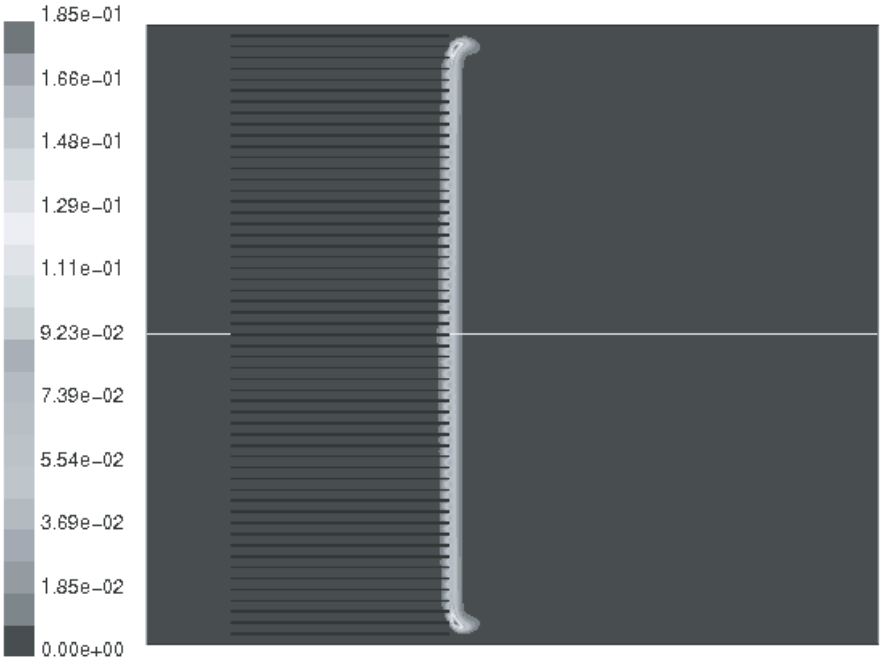

Figure 4.13: Computed reaction rate contours downstream of the Rijke tube honeycomb

contours show the presence of the flame front on top of the honeycomb. As can be observed in the figure, the flame sits right on top of the honeycomb (less than $1\,mm$ downstream of the honeycomb outlet). The preheating of air-fuel mixture is shown in Figure 4.14. The temperature contours show the incoming air-fuel mixture gets preheated to around $800\,K$ at the outlet of the honeycomb. The temperature contours indicate convective heat transfer from the cordierite wall to the air-fuel mixture. The overall heat transfer process in the preheating of the incoming mixture can be explained as follows:

- heat is transferred to the top surface of the honeycomb from the flame,
- an axial temperature distribution inside the cordierite walls occurs because of conductive heating through the solid,
- heat is transferred to the colder mixture entering the honeycomb convectively and as the mixture passes through the honeycomb passages, more heat is added which results

in a much higher temperature of the mixture at the honeycomb outlet.

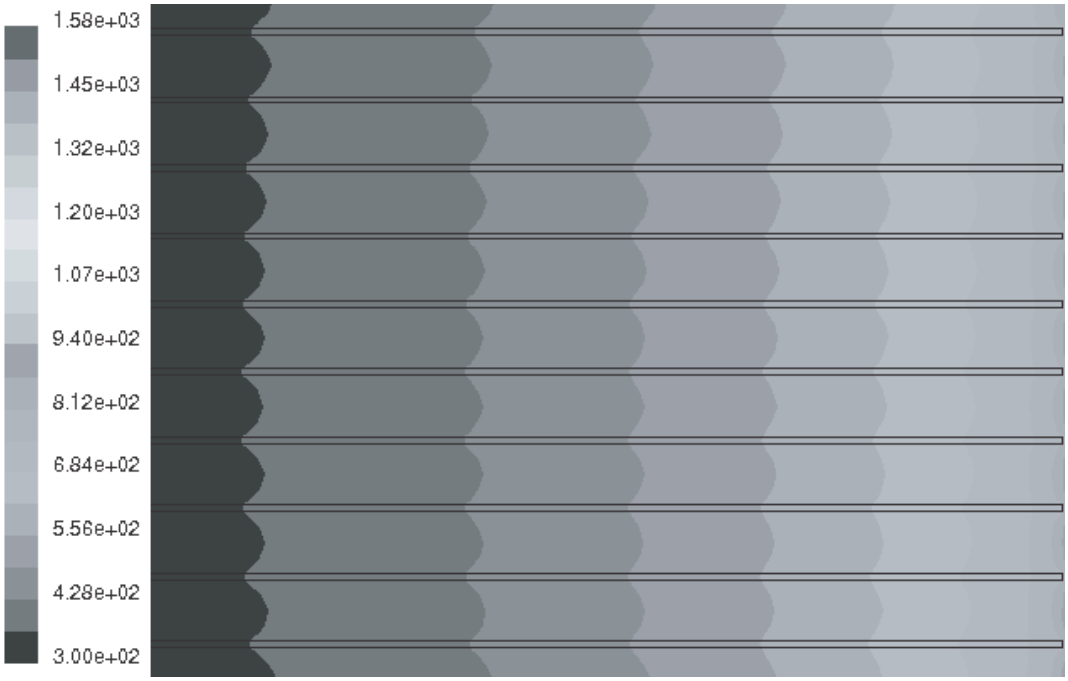

Figure 4.14: Preheating of air-fuel mixture inside the Rijke tube honeycomb channels

The flat flame shows curling at the edges (as can be seen in Figure 4.13). This phenomena occurs because of the heat loses at the wall. The heat generated by the flame is lost to the surrounding through the carbon steel wall and subsequent reduction in temperature takes place next to the wall surface. This results in the flame getting detached from the wall surface and curls.

Combustion Products Formation

The single-step chemistry model documented in Section 4.4.3 is responsible for the prediction of products formation (CO_2 and H_2O) in the model. Figure 4.15 shows the axial mole fraction distribution of the species along the centerline. The reaction rate curve shows the position of the flame and the thick vertical line shows the outlet of the honeycomb.

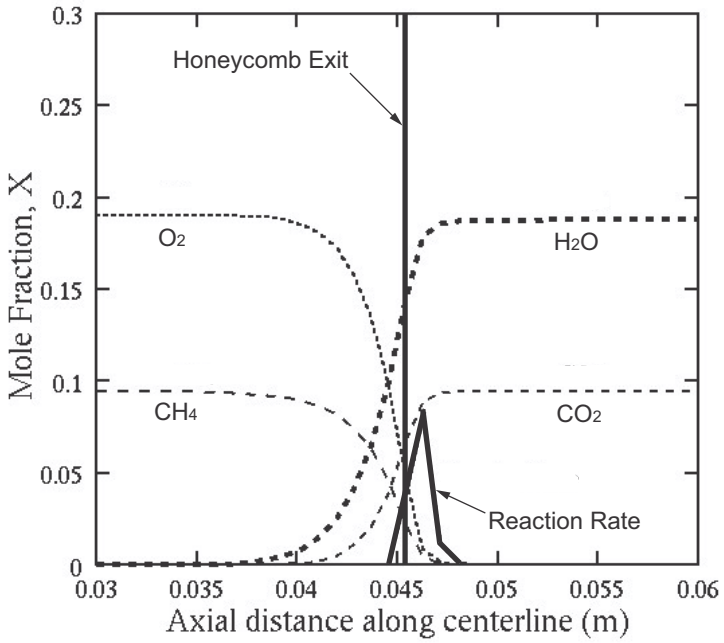

Figure 4.15: Rijke tube simulation axial mole fraction distribution inside the honeycomb and at its immediate downstream

The flame position can be estimated from the figure to be around $1.25\,mm$ downstream from the outlet of the honeycomb. The fuel is completely consumed immediately downstream of the flame and both O_2 and CH_4 mole fractions become zero. The products formation starts around $7.5\,mm$ upstream of where the reaction rate maxima occurs and is associated with the destruction of the fuel and oxidizer which also begins at the same location. The steady state mole fraction distribution shows the exact location of the flame with respect to the honeycomb top surface and also proves the effectiveness of the chemistry model in predicting the species distribution.

Temperature Distribution

In Figure 4.16 temperatures predicted along the axis are shown along with experimentally measured temperatures. The maximum temperature predicted ($1146.67\,K$) occurs immedi-

ately downstream of the honeycomb exit. The maximum temperature predicted is approximately 200 K higher than the measured experimental temperature. For example, it can be seen in the figure that at 1.82 cm downstream of the honeycomb, the measured temperature is 954.25 K (the second circle from the left) whereas the predicted temperature is around 1130 K. Since very little heat is lost from the products to the atmosphere, the prediction of temperatures near the honeycomb top surface should have been more accurate. The accuracy of temperature prediction is directly related to the accuracy of modeling the chemical dynamics of the reacting flow. The single-step chemistry model, although is able to predict the flame location accurately (as described in the previous section), tends to over predict temperatures. Prohibitive computational expenses (long computation times) restricted the study to single-step chemistry modeling. It should be noted here that the experimentally measured temperatures do not include radiation correction and therefore should be higher than the displayed values.

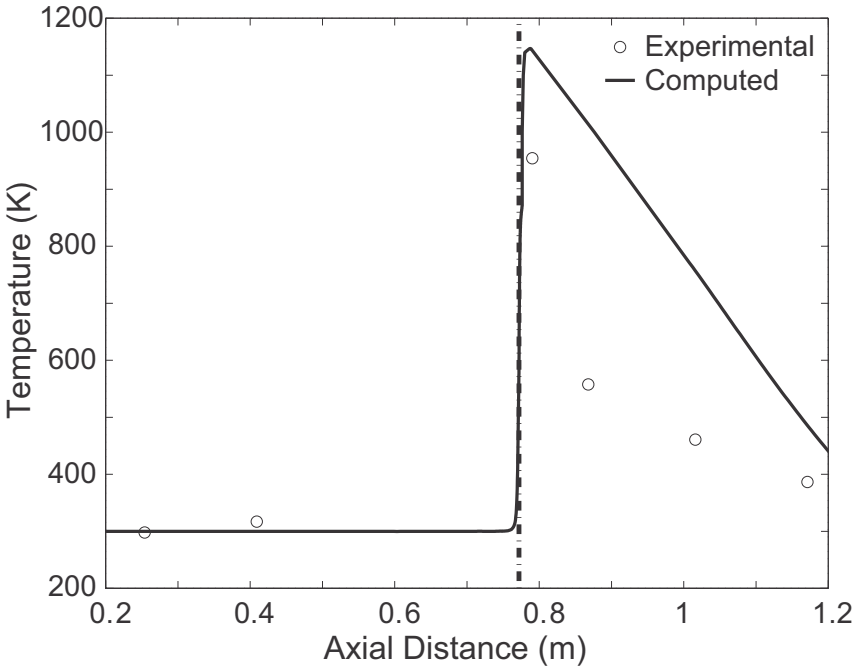

Figure 4.16: Rijke tube simulation axial temperature distribution along the centerline ($x = 0$ at combustor inlet)

For the experimental temperature values it can be noted that there is a steep temperature gradient downstream of the honeycomb (till around $0.875\,m$) and later the temperature gradient falls. The initial steep gradient is indicative of the contribution of radiation heat transfer in the overall heat transfer process. The predicted temperature gradient downstream of the honeycomb is uniform and does not show the rapid decrease in temperature due to radiation heat transfer.

4.5.2 Dynamic Characteristics of the Combustor

To capture the dynamic characteristics of the combustor, time-accurate integration of the transport equations was carried out. Two different regimes are present in the unsteady simulation:

1. The exponential growth of the instability
2. Subsequent limit-cycle behavior

Capturing the growth of the instability is of primary importance for the model. The instability growth mechanism should be captured because of accurate flow and heat transfer modeling and accurate boundary conditions. Boundary conditions, in particular, are important because inaccurate boundary conditions will not enable the prediction of the unstable regime of the combustor correctly. Therefore, non-reflecting boundary conditions were chosen so that at the inlet a velocity node and a pressure anti-node are present and at the outlet acoustic energy losses are maximized so that acoustic/flame coupling is minimized. The pressure anti-node at the inlet and the node at the exit of the combustor can be seen in Figure 4.17. The figure shows instantaneous axial pressure distribution along the centerline of the combustor. For the tube combustor, the second acoustic mode is excited and exhibits a limit-cycle. The shape of the curve indicates a three-quarter mode shape. The pressure maximum occurs downstream of the honeycomb (at the $1\,m$ location), which matches the theoretical pressure maxima location for a three-quarter wave form.

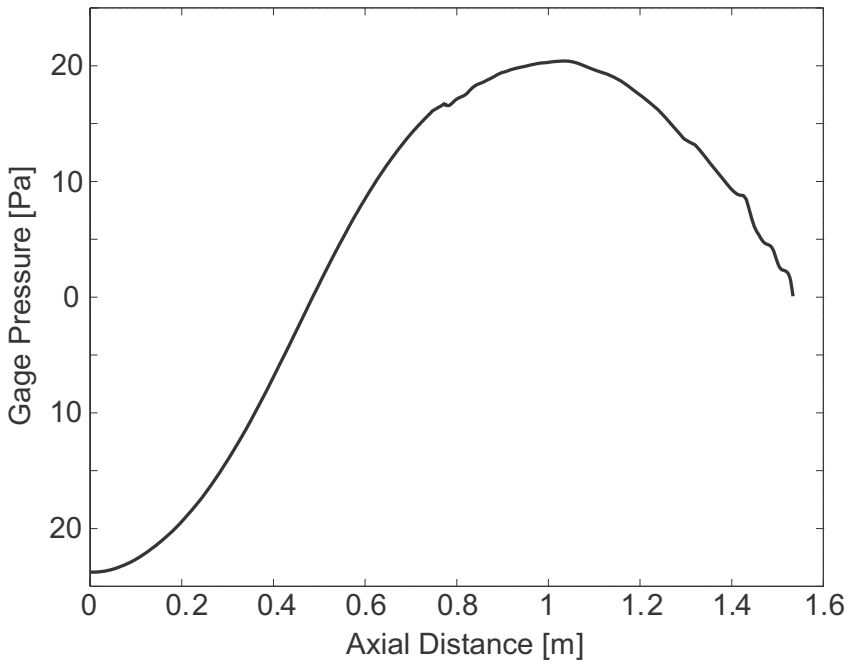

Figure 4.17: Rijke tube simulation pressure mode shape for the second acoustical mode of the tube

The following sections document the observations in the two regimes – the growth of instability regime and the subsequent limit-cycle behavior.

Growth of Instability

The instability growth mechanism is characterized by increasing oscillations of pressure inside the combustor. The growth can be observed in Figure 4.18, which shows the growth of unsteady pressure $5\,cm$ downstream of the honeycomb. At approximately $0.2\,s$ after the time-integration was initialized, the pressure starts oscillating. This oscillation grows till about $0.4\,s$ and then subsides to a limit-cycle behavior. Once limit-cycle is reached, the pressure has a fixed mean amplitude of oscillation. The amplitude is only affected by the other dynamics of the combustor – effect of pulsating instability, for example.

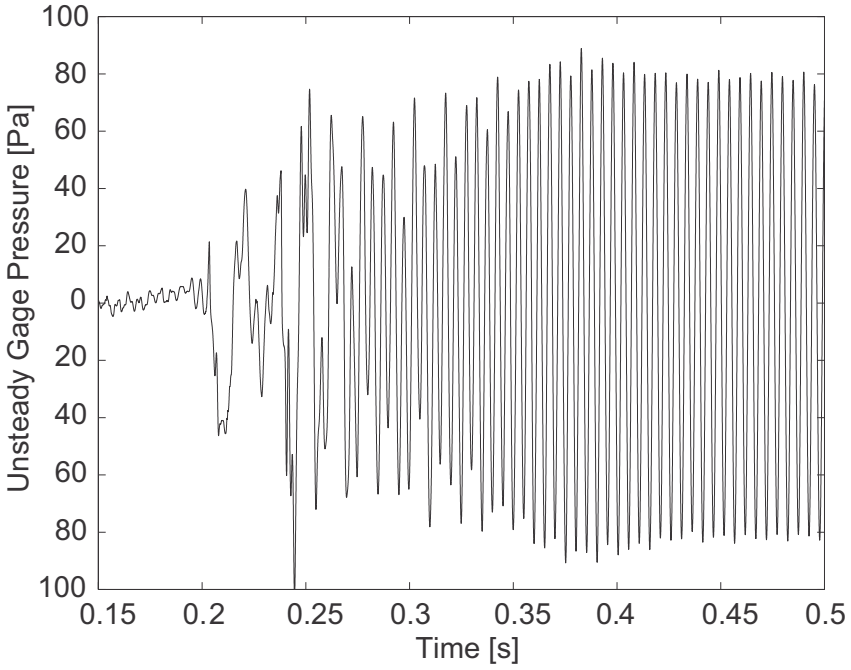

Figure 4.18: Growth of unsteady pressure in the Rijke tube (computed results)

Limit-Cycle and Pressure Power Spectrum

The limit-cycle behavior of the unsteady pressure inside the combustor is illustrated in Figure 4.19. The figure shows the unsteady normalized (by the mean pressure) pressure at $5\,cm$ downstream of the honeycomb plotted against time. The pressure oscillates at $187\,Hz$ which can be observed in Figure 4.20. This figure shows the power spectrum of unsteady pressure fluctuation shown in Figure 4.19. The power spectrum is generated using a sampling rate of 8192 (corresponding to a time step of $1.2207 \times 10^{-5}\,s$) and no averaging techniques have been implemented. The power spectrum has been calculated from $1.5\,s$ of computed data for $\phi = 1.0$ and $Q = 120\,cc/s$. The spectrum shows that following characteristics of the acoustic signature of the combustor have been captured:

- The fundamental frequency corresponding to the three-quarter mode of the combustor has been captured to be $187\,Hz$. The magnitude of the peak at $187\,Hz$ is approximately

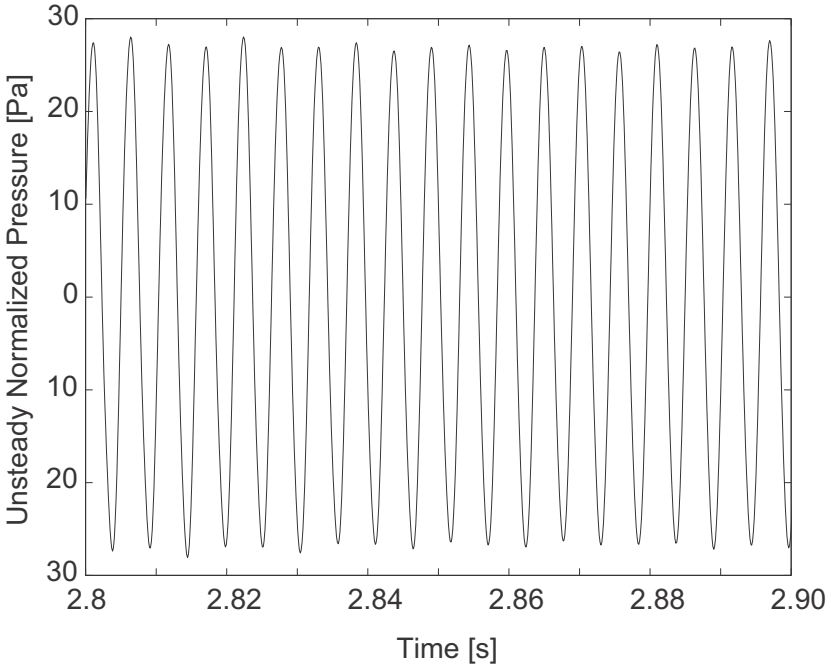

Figure 4.19: Time trace of the unsteady pressure oscillation in the Rijke tube combustor (computed results)

$120\,dB$.

- The first four harmonics of the fundamental frequency are visible at $374\,Hz$, $561\,Hz$, $748\,Hz$ and $935\,Hz$.
- A peak at around $70\,Hz$ can be observed. This peak does not match with the experimentally observed peak at $90\,Hz$ (half the fundamental frequency).

Although the fundamental frequency at which the instability occurs and its harmonics have been predicted, two major features of the power spectrum which were observed in the experimental studies (subharmonic response and the pulsating instability) have not been captured by the model explicitly. It will be shown in the following section that averaging methods applied to the data make the pulsating instability mechanism visible in the spectrum, although the subharmonic instability that was observed in experiments to happen around $90\,Hz$ has

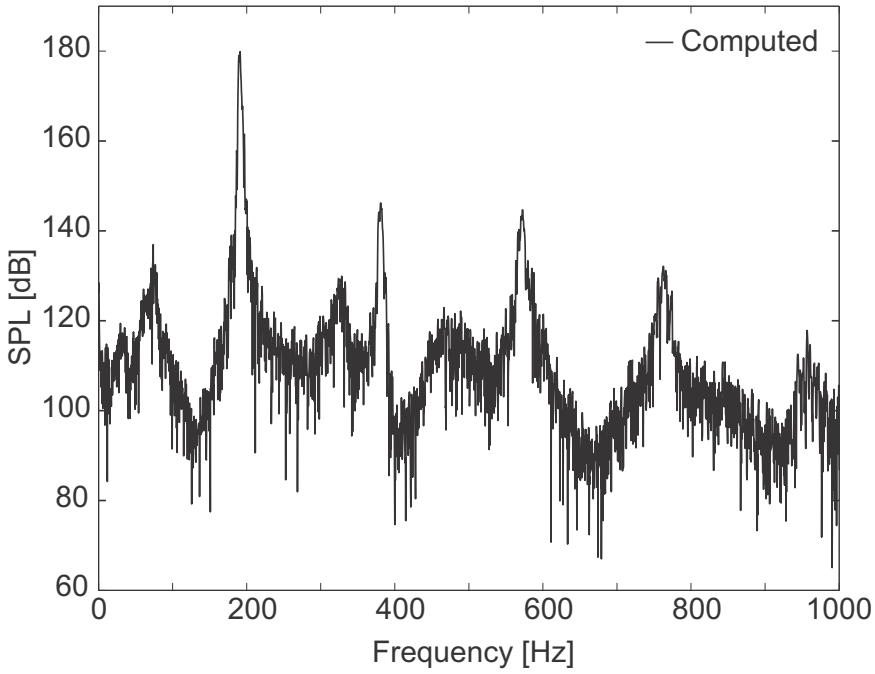

Figure 4.20: Pressure power spectrum from the Rijke tube simulation, showing limit-cycle

not been predicted by the model. The reasons for failure can be attributed to the inability of the model to capture the mode-shape featuring mechanism of the flame which was observed in the experimental studies. Two alternate and independent reasons can be given as an explanation of the peak observed at $70\,Hz$ in the computational study:

1. Using a finite element method (FEM) to calculate the modes of the combustor for cold flow, Nord [48] showed that the first mode of the combustor existed at $63\,Hz$ and the second occurred at $166\,Hz$. The second acoustic mode (the 3/4 mode) gets excited for the reacting flow in the combustor and is observed at $182\,Hz$ in the experiments. It can be assumed that the computational results over-predict the first acoustic mode of the system as compared to the damped mode seen in experimental results. The frequency at which the first mode is predicted ($70\,Hz$) is higher than the $63\,Hz$ cold acoustic calculations because of the presence of higher temperatures in the combustor (hot acoustics).

2. An alternate explanation for the $70\,Hz$ peak can be that the model has been able to predict the subharmonic peak but tends to under predict the frequency by $20\,Hz$. In the experimental studies, a question was raised as to whether the subharmonic instability is dependent on the limit-cycle amplitude or the limit-cycle frequency. It was suggested that the flame sheet has preferred frequencies which can be seen as resonances of the flame and are observed as the subharmonic peak in the pressure power spectrum. The failure to predict such a 'preferred' frequency in the $\phi = 1.0$ and $Q = 120\,cc/s$ simulation by the computational model may result in the under prediction of the subharmonic instability.

As will be discussed later, the second explanation is probably not true and the $70\,Hz$ peak is the first mode of the combustor which is over predicted.

The Pulsating Instability

A closer look at the limit-cycle pressure oscillation (Figure 4.19) reveals the presence of frequencies other than the fundamental. Included in these multiple frequencies, along with the harmonics of the fundamental (at $187\,Hz$), is the pulsating instability (mentioned in Section 4.3) which results in amplitude modulation of the fundamental frequency and the harmonics and is visible in the form of sidebands on the frequency peaks. In Figure 4.20, the pressure power spectrum shown is obtained without averaging the data. Upon using averaging methods available in MATLAB, the pulsating instability occurring in the combustor can be captured. A Hanning window method was used to average the data ($1.5\,s$ of data) and a sliding window was applied. The sliding window was needed to take care of the sparse data set (less than $2\,s$ of data used). Figure 4.21 shows the pressure power spectrum obtained with the averaging techniques implemented. Sidebands on the fundamental frequency and the subsonic pulsating instability are marked on the figure.

As seen in Figure 4.21, the pulsating instability can be seen around the subsonic region and is measured to be $24\,Hz$. The sideband locations on the fundamental frequency are

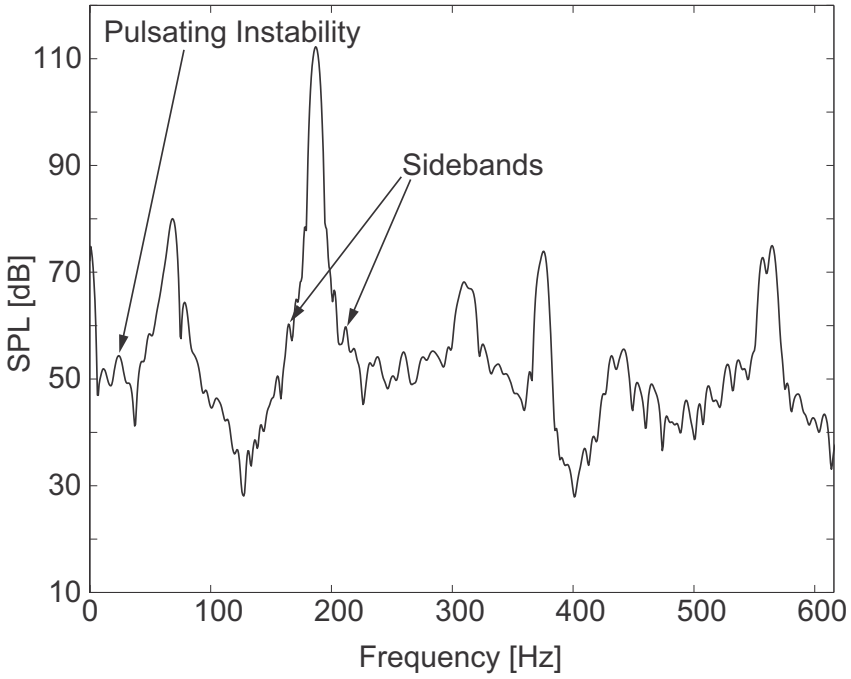

Figure 4.21: Amplitude modulation and the subsonic instability from Rijke tube simulation

$187 \pm 24\,Hz$ and can be seen in Figure 4.22. The pulsating instability is a direct result of the flame-honeycomb heat transfer coupling and is successfully captured by the model.

4.5.3 Comparison with Experimental Results

The computed pressure power spectrum for $\phi = 1.0$ and $Q = 120\,cc/s$ is compared with the power spectrum generated from experimental results. Data used for the computed pressure power spectrum corresponds to a simulation time of $3.5\,s$. The Hanning sliding window available in MATLAB has been used for averaging the data. In Figure 4.23, the thermoacoustic instability is predicted to occur at $187\,Hz$ as compared to $182\,Hz$ measured in the experiments. The computed magnitude is $178\,dB$ whereas the experimental value calculated is $177\,dB$. The magnitude over prediction by the model can be attributed to the outlet acoustic boundary condition. Although, the attempt has been to implement accurate acous-

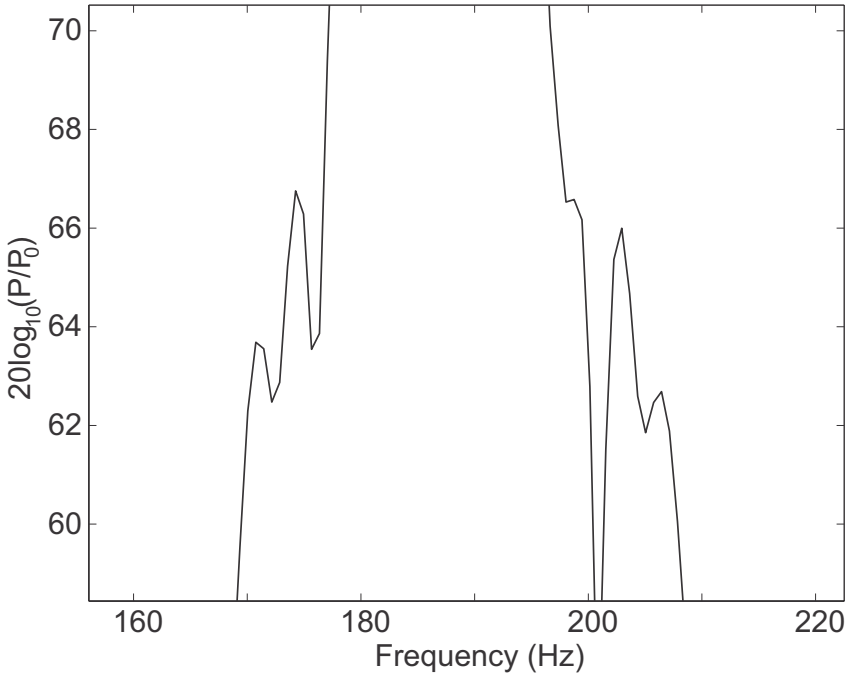

Figure 4.22: Sidebands on the fundamental frequency peak from the Rijke tube simulation

tic boundary condition at the combustor outlet, it has not been possible to account for the acoustic radiation condition where part of the acoustic energy is radiated out and part of it is reflected back inside the combustor. Accurate transmission and reflection conditions need to be implemented to get a better match between experimental and computed limit-cycle magnitudes.

As can be seen in Figure 4.23, the subharmonic frequency (expected at $91\,Hz$, half of the fundamental $182\,Hz$) is not visible in the experimental pressure power spectrum. Thus, the $70\,Hz$ peak that can be observed in the computed power spectrum can not be the under predicted subharmonic frequency (as discussed in Section 4.5.2). It can therefore be hypothesized that the $70\,Hz$ frequency is indeed the first-mode of the combustor which was over predicted. The difference between the predicted cold-acoustics value of $63\,Hz$ and the computed $70\,Hz$ hot-acoustics value is as expected since frequencies obtained in hot-acoustics are usually higher as compared to the cold-acoustics values.

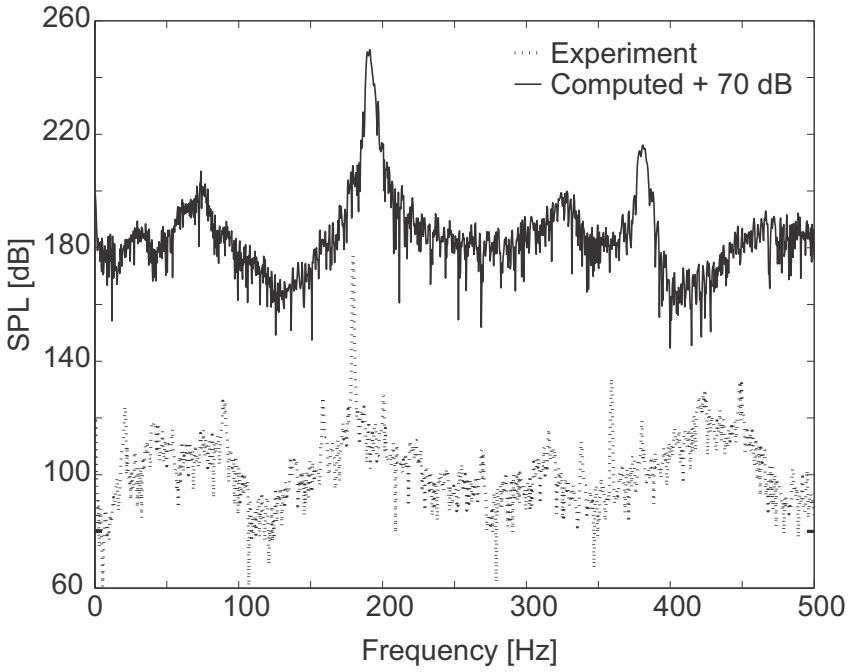

Figure 4.23: Rijke tube combustor: comparison between computed results and experimental results

4.6 Summary

Two dimensional CFD modeling of the Rijke tube combustor geometry was performed. The growth of the self-excited instability to limit cycle behavior was captured by the model. The pressure power spectrum of the limit cycle oscillation showed that the instability mechanism is highly nonlinear. Several distinct features were observed in the power spectrum – the fundamental was predicted at $187\,Hz$, the harmonics of the fundamental frequencies were visible and a low frequency pulsating instability was also observed. This low frequency instability was observed to modulate the amplitude of the fundamental frequency. Investigation of the coupling between the heat release rate and the effect of upstream velocity oscillations was carried out, and is presented in Chapters 5 and 6.